nuclear fusion
IAEA

PAPER • OPEN ACCESS

Recent advance progress of HL-3 experiments

To cite this article: X.R. Duan *et al* 2024 *Nucl. Fusion* **64** 112021

View the article online for updates and enhancements.

You may also like

- Physics basis for the divertor tokamak test facility
F. Crisanti, R. Ambrosino, M.V. Falessi et al.
- The effect of shaping on trapped electron mode stability: an analytical model
X. Garbet, P. Donnel, L. De Gianni et al.
- Negative triangularity scenarios: from TCV and AUG experiments to DTT predictions
A. Mariani, L. Aucone, A. Balestri et al.

This content was downloaded from IP address 192.107.52.20 on 03/04/2025 at 09:10

OPEN ACCESS
IOP Publishing | International Atomic Energy Agency
Nuclear Fusion
Nucl. Fusion **64** (2024) 112021 (14pp)
https://doi.org/10.1088/1741-4326/ad6e9e

Recent advance progress of HL-3 experiments

X.R. Duan[1,*], M. Xu[1], W.L. Zhong[1], X.Q. Ji[1], W. Chen[1], Z.B. Shi[1], X.L. Liu[1], B. Lu[1], B. Li[1], Y.Q. Wang[1], J.Q. Li[1], G.Y. Zheng[1], Yong Liu[1], Q.W. Yang[1], L.W. Yan[1], L.J. Cai[1], Q. Li[1], Y. Liu[1], X.Y. Bai[1], Z. Cao[1], X. Chen[1], H.T. Chen[1], Y.H. Chen[1], G.Q. Dong[1], H.L. Du[1], D.M. Fan[1], J.M. Gao[1], S.F. Geng[1], G.Z. Hao[1], H.M. He[1], M. Huang[1], M. Jiang[1], R. Ke[1], A.S. Liang[1], J.X. Li[1], Qing Li[1], Yongge Li[1], L.C. Li[1], H.J. Li[1], W.B. Li[1], D.Q. Liu[1], T. Long[1], L.F. Lu[1], L. Nie[1], P.W. Shi[1], J.F. Peng[1], A.P. Sun[1], T.F. Sun[1], R.H. Tong[1], H.L. Wei[1], S. Wang[1], G.L. Xiao[1], X.P. Xiao[1], L. Xue[1], H.B. Xu[1], Z.Y. Yang[1], D.L. Yu[1], L.M. Yu[1], Y.P. Zhang[1], X. Zheng[1], L. Zhang[1], Y. Zhang[1], F. Zhang[1], X.L. Zhang[1] and HL-3 Team & Collaborators[2,3,4,5,6,7,8,9,10,11,12,13,14,15,16,17,18,19]

[1] Southwestern Institute of Physics, PO Box 432, Chengdu 610041, China
[2] CEA, IRFM F- 13108 Saint-Paul-lez-Durance, France
[3] Department of Physics, Zhejiang University, Hangzhou 310058, China
[4] Department of Physics and Astronomy, University of California, Irvine, CA 92697-4575, United States of America
[5] Department of Engineering Physics, Tsinghua University, Beijing 100084, China
[6] Dalian University of Technology, Dalian 116024, China
[7] National Institute for Fusion Science, 322-6 Oroshi-cho, Toki-shi 509-5292, Japan
[8] General Atomics, PO Box, San Diego, CA 85608, United States of America
[9] University of Wisconsin-Madison, Madison, WI, United States of America
[10] Institute of Fusion Science, School of Physical Science and Technology, Southwest Jiaotong University, Chengdu 610031, China
[11] University of Science and Technology of China, Hefei 230026, China
[12] Center for Nonlinear Plasma Science and ENEA C. R. Frascati, Via E. Fermi 45 00044 Frascati (Roma), Italy
[13] University of California San Diego, San Diego, CA, United States of America
[14] Huazhong University of Science and Technology, Wuhan 430074, China
[15] University of South China, Hengyang 421001, China
[16] Peking University, Beijing 100871, China
[17] Princeton Plasma Physics Laboratory, Princeton, NJ, United States of America
[18] Durham University, Durham, United Kingdom of Great Britain and Northern Ireland
[19] Harbin Institute of Technology, Harbin 150001, China

E-mail: duanxr@swip.ac.cn

Received 15 January 2024, revised 12 June 2024
Accepted for publication 13 August 2024
Published 2 September 2024

Abstract

Since the first plasma realized in 2020, a series of key systems on HL-3 (known as HL-2M before) tokamak have been equipped/upgraded, including in-vessel components (the first wall, lower divertor, and toroidal cryogenic/water-cooling/baking/glow discharge systems, etc.), auxiliary heating system of 11 MW, and 28 diagnostic systems (to measure the plasma density,

* Author to whom any correspondence should be addressed.

Original content from this work may be used under the terms of the Creative Commons Attribution 4.0 licence. Any further distribution of this work must maintain attribution to the author(s) and the title of the work, journal citation and DOI.

electron temperature, radiation, magnetic field, etc.). Magnet field systems were commissioned firstly for divertor plasma discharges. During the 2nd experimental campaign of HL-3 tokamak, several great progresses have been achieved. Firstly, the successful operation with plasma current larger than 1 MA was achieved under a divertor configuration. Secondly, the advanced divertor concept with two distinct snowflake configurations was realized. It is found that the distribution of ion saturation current and heat flux on bottom plate becomes wide due to magnetic surface expansion, demonstrating the advantage of such configuration in the heat flux mitigation. In addition, using the combination of NBI, ECRH and LHCD, the standard sawtoothing high confinement mode of megampere plasma was firstly accessed on the HL-3. The successful commissioning of HL-3 is beneficial for the initial operation of ITER.

Keywords: tokamak, HL-3 experiment, 1 MA plasma, advanced divertor, H-mode

(Some figures may appear in colour only in the online journal)

1. Introduction

Recently, the new tokamak known as HL-2M before has been officially renamed as HL-3. The design parameters are as follows: plasma current $I_p = 2.5 \sim 3$ MA, toroidal field $B = 2.2 \sim 3$ T, major radius $R = 1.78$ m, minor radius $a = 0.65$ m, elongation $\kappa \leqslant 1.8$, triangularity $\delta \leqslant 0.5$. The HL-3 research programme focuses on key issues in the development of advanced divertor concepts and high heat flux components, as well as the high-performance operation scenarios in support of ITER and next fusion reactors [1–8].

Since the first commissioning of HL-3 in 2020, numerous in-vessel components have been installed/upgraded in order to achieve the 1 MA discharge during the second experimental campaign, including the first wall, the lower divertor, the toroidal cryogenic, water-cooling, baking and glow discharge systems, etc. Up to now, the capability of auxiliary heating & current drive system has been improved to 11 MW, including the NBI of 5 MW, ECRH of 4 MW, and LHCD of 2 MW. Moreover, a comprehensive set of diagnostic system has been installed to measure the key parameters of plasma, such as the plasma density, electron temperature, radiation, magnetic field, and plasma current. Especially, a heterodyne interferometer was equipped with a phase processor, used to the feedback control of electron density in real time. A frequency modulated continuous wave reflectometer was developed to measure the density profiles. A 60 channel-electron cyclotron emission (ECE) radiometer, with quasi-optical system inside the vessel and ITER-like long-distance corrugated waveguide, was utilized to measure the electron temperature profiles. Two sets of Thomson scattering diagnostic systems (core region with laser 50 Hz/3 J, edge with laser 30 Hz/2 J) were applied for density and electron temperature profile measurements. As for fueling, four sets of gas injection systems were used to the density feedback control. Meanwhile, three sets of supersonic molecular beam injection (SMBI) systems were fabricated, including a high-field side system and a divertor heat flux control one. A new pellet injection system was finished, which could inject cylindrical pellets with the diameter of 1.0 mm and the length of 1.0–1.3 mm. This system is able to operate at a frequency of 60 Hz and an adjustable speed at 100–300 m s^{-1}. To ensure good wall conditioning, HL-3 vacuum vessel and all in-vessel components were baked at a temperature of 135 °C sustained for more than 10 d to degas water vapor, and then the glow-discharge cleaning (GDC) with helium was employed to remove the impurities such as oxide, carbide, etc.

In the 2nd experimental campaign from 2022–2023, a series of operation milestones of HL-3 were realized. Firstly, the successful operation with the plasma current larger than 1 MA was achieved under a divertor configuration. Secondly, advanced divertor concept—snowflake (SF) configuration was realized. In addition, combined with NBI, ECRH and LHCD, the standard sawtoothing high confinement mode of megampere plasma was firstly accessed. These will be shown in the following sections 2–4. Summary and next research plan will be drawn in section 5.

(Parallel to HL-3 debugging experiments, HL-2 A tokamak has made significant progress in exploring plasma physics, especially on the development of advanced operation scenarios, energetic particle physics, turbulence, divertor detachment, etc. Referring to [9–18].)

2. Megampere plasma discharge

For the engineering safety, the toroidal magnetic field employed during this campaign was maintained at 1.5 T. A plasma configuration with an elongation of 1.4 was deliberately chosen. Remarkably, within just one month of the campaign's commencement in 2022, HL-3 team achieved a megampere plasma with a low q discharge, consistently maintaining a q_{95} value around 2.5 throughout the experiment. Figure 1 displays the key parameters and plasma equilibrium reconstructed with EFIT. Plasma current experienced a rapid increase, peaking at nearly 1.2 MA with a ramp-up rate of 1 MA s^{-1}. Unfortunately, this limiter plasma had to be terminated due to constraints imposed by the available volt-seconds in the 2nd experimental campaign (the central solenoid coil current ranged from +60 kA to −100 kA). However, the divertor plasma with lower Z_{eff} and radiated power at the same volt-seconds allows to realize a stable plasma current of 1 MA.

As the plasma current has reached the megampere level, the risk of disruption is the key issue for HL-3. In order to

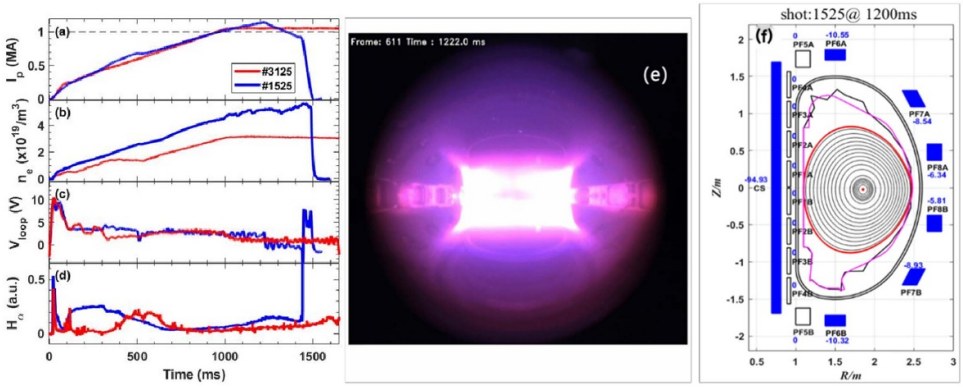

Figure 1. The first megampere plasma discharge on HL-3. Shot #1525 (blue curve) and #3125 (red curve) correspond to the limiter and divertor configuration respectively. (*a*)–(*d*) waveforms of the plasma current, electron density, loop-voltage and H_α for shot 1525 and 3125, (*e*) and (*f*) the limiter plasma image and configuration from CCD camera and EFIT for shot 1525, respectively.

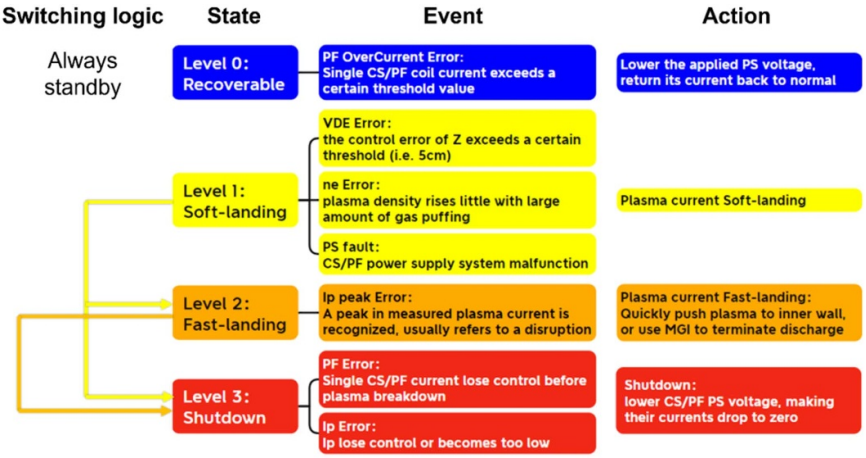

Figure 2. Structure of HL-3 abnormal event handling system: states, events, actions to be taken and the switching logic among states.

guarantee operation safety, an off-normal event handling system has been developed. The system utilizes a finite-state-machine concept to classify different off-normal events into several states according to their impacts on the discharges, which are then used to determine what actions should be taken to handle the events, as shown in figure 2. For instance, during the initial stages of diverted plasma commissioning, HL-3 suffered some vertical displacement events (VDEs), which typically occur within a few milliseconds and are well known to generate significant electromagnetic forces probably leading to the HL-3 damage. However, this challenge was effectively addressed by the off-normal event handling system, which promptly detected a 'VDE error' signal and transitioned the plasma into a controlled soft-landing phase. In the experiments in 2023, potential VDEs in hundreds of discharges for $I_\mathrm{p} = 0.3$–1.1 MA have been avoided. As an emergency method to reduce disruption risks, once the VDE is unavoidable, disruption mitigation system based on the massive gas injection (MGI) will be triggered by off-normal event handling system in real-time.

Meanwhile, HL-3 also explored the application of machine learning (ML) techniques for disruption prediction [19]. Its implementation can be divided into two steps.

(1) Building a disruption prediction dataset as reproducible and comprehensive as possible, which could serve as a simulated development platform for algorithms. Up to now, a preliminary dataset consisting of about 1200 shots has been collected. The content of dataset is not limited to diagnostic signals and disruption labels. It also contains the event chain before disruptions, the adjustment of hardware systems and operating strategies, and the key impact of disruptions.

(2) Implementing deep learning-based disruption predictor to further validate these new techniques. A surrogate model of EFIT has been developed by using deconvolutional neural network, the VDE and all types of disruption predictors based on temporal recurrent neural network (TCN). As conducted on HL-2A [19], the VDE predictor has been real-timely implemented into the plasma control system to trigger an MGI before VDE disruptions on HL-3. Figure 3 shows the structure, input list and an output example of the VDE predictor. Figure 4 shows the receiver-operator characteristic (ROC) curve and the area under ROC curve (AUC) of the two predictors. It seems that the data requirement of multi-type disruption predictor is higher than single-type algorithms.

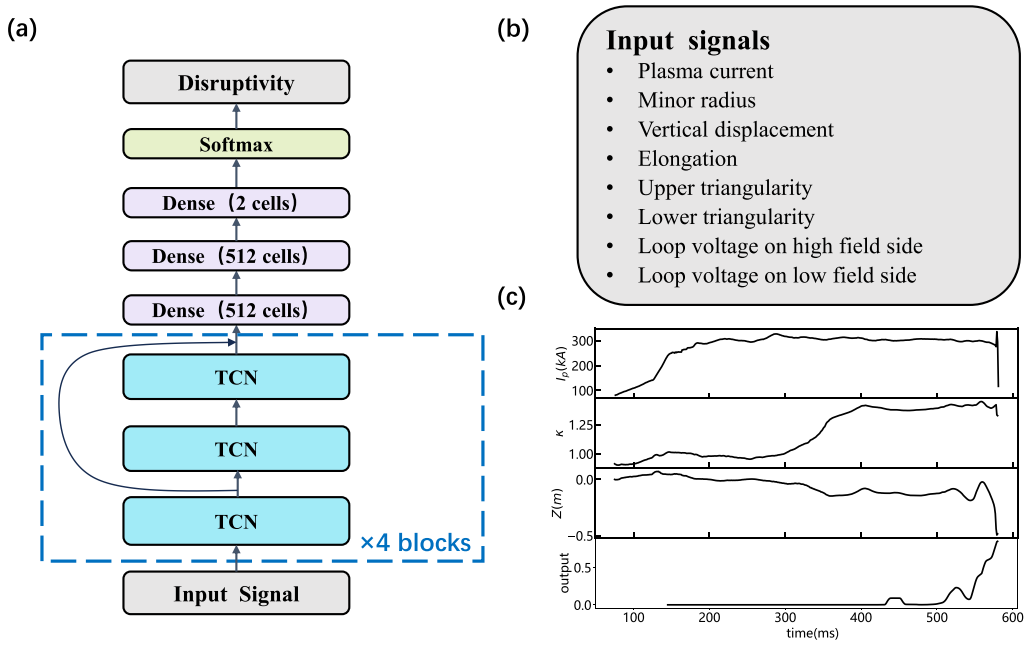

Figure 3. (*a*) Structure of the neural network to predict VDE, which consists of several temporal convolutional networks (TCN), several dense connected layers and a softmax activation layer. (*b*) Input signal list of the VDE predictor. (*c*) The plasma current, elongation, vertical displacement and output of VDE predictor during shot 3426 of HL-3.

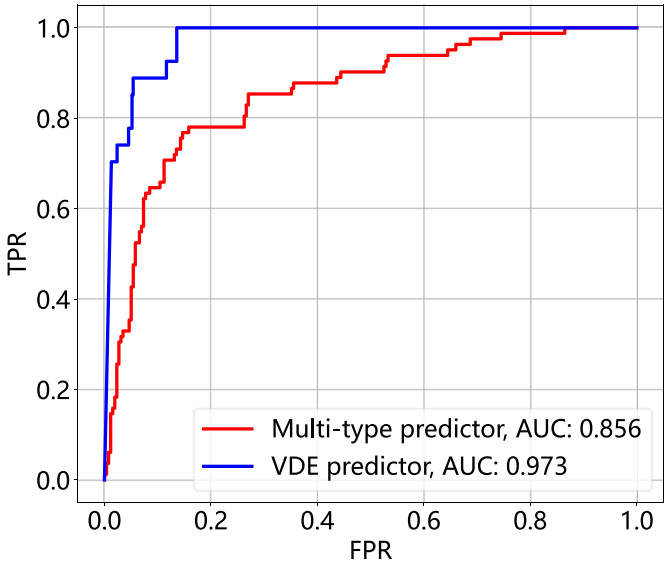

Figure 4. Receiver-operator characteristic curves of the VDE and the multi-type disruption predictors. The *x*-axis and *y*-axis are false or true positive rates of the models tested during shots 3200–4100, 352 valid shots in HL-3.

The preliminary results validated the efficiency of ML techniques, but there were still a series of engineering problems to be solved. The HL-3 team will keep working on the dataset and algorithm development, to accumulate the experiences for developing disruption prediction algorithms.

In 2023, reproducible divertor plasma discharges with $I_p \geqslant 1$ MA and elongation of 1.5 were achieved on HL-3. As shown in figure 5, the line-averaged electron density reached $4.4 \times 10^{19}\,\mathrm{m}^{-3}$, which was about 57% of the Greenwald limit. The transition from limiter to divertor configuration in the ramp-up phase occurred between 260 and 360 ms. Subsequently, the plasma current was gradually raised at a rate of 1 MA s^{-1}, resulting in a flat-top current of 1.05 MA, sustainable for 600 ms. Edge plasma safety factor q_{95} ranged from 2.6 to 3.4 during the 1 MA divertor discharges. It demonstrates that high performance plasma can be robustly achieved without major disruption; even when q_{95} is a little lower than 3.0.

3. Advanced divertor conception test

Testing advanced divertor concepts for fusion reactors represents a primary mission of HL-3. During the 2nd campaign, the team explored two distinct advanced divertor configurations, namely the SF-minus (SF−) and SF-plus (SF+) [20–23]. Main parameters of the configurations are as follows: plasma current $I_p = 500$ kA, the major radius $R = 1.78$ m, the minor radius $a = 0.62$ m, the elongation $k = 1.5$ and the triangularity $\delta = 0.52$. In the SF- configuration, the secondary X-point was strategically positioned in scrape-off layer (SOL), and the distance between the primary and secondary X-point $D_{x12} = 30$ cm, as shown figure 6(*a*). The magnetic field flux surface in the outer divertor leg of the SF− configuration was significantly expanded, so that the magnetic field lines of the SOL covered bottom region, which would increase wet area and help to reduce the peak heat load on target plate. By optimizing the current combination of divertor coils, the secondary X-point was moved to the private flux region, resulting in the configuration transformation from the SF− to SF+, as depicted in figure 6(*b*). The primary configuration parameters of SF− and SF+ remained nearly identically, except for the

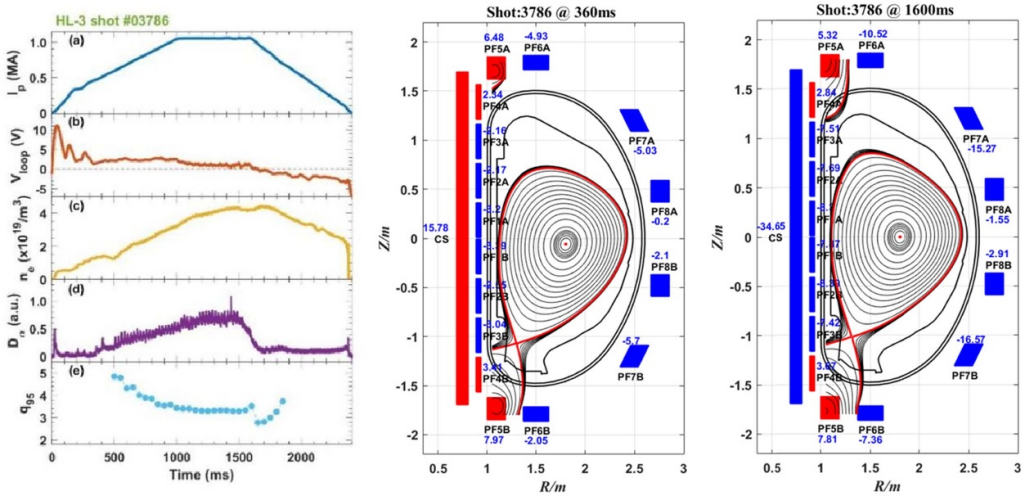

Figure 5. Mega-ampere discharge characteristics with divertor configurations. (*a*) Plasma current, (*b*) loop voltage, (*c*) line-averaged electron density, (*d*) $D\alpha$ intensity, and (*e*) the safety factor at 95% flux surface q_{95} in the left panels. Divertor configurations at 360 ms and 1600 ms reconstructed from EFIT code in the middle and right panels.

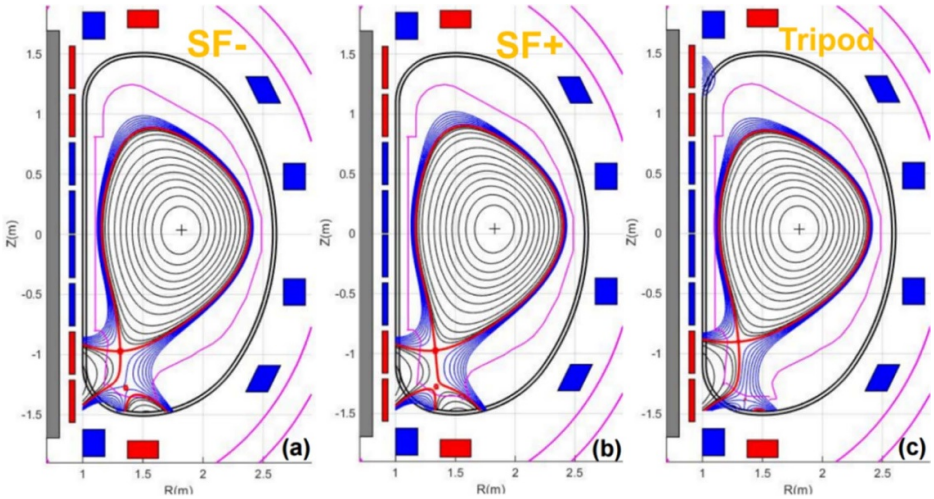

Figure 6. Typical advanced divertor configuration of HL-3, (*a*) snowflake-minus (SF−), (*b*) snowflake-plus (SF+), and (*c*) tripod.

distinct locations of their secondary X-points. This deliberate variation in the secondary X-point allowed for a comprehensive study of the unique characteristics exhibited by SF− and SF +. In contrast, the tripod configuration [24] still featured a substantial flux expansion in the outer divertor leg, with a D_{x12} distance up to 50 cm, as shown figure 6(*c*).

In 2023, these advanced divertor configurations were first realized in experiments. They were confirmed by both the image of the fast camera and EFIT equilibrium reconstruction. In contrast, the image of the standard single-null (SN) configuration possessed two crystal clear bright rings on the divertor target, as shown in figure 7(*a*), corresponding to the inner and outer strike points of the SN configuration, see figure 7(*b*). For the advanced configuration, the ring of the outer strike point became a light band on the bottom target due to the expansion of magnetic flux surface, see figure 7(*c*). This was also an essential feature of advanced divertor configurations.

Besides, the distinction between SF− and SF+ configurations could be discerned through both an infrared/visible imaging system and divertor flush probes. An imaging system, capable of operating in both visible and infrared wavelengths, was developed for in-vessel inspection [25, 26], as depicted in figure 8. The ion saturation current from the divertor target probes analogous on HL-2A [27] during shot 4177 is presented in figure 9. Here, the horizontal axis is time, while the vertical axis represents the arc length along the target plate probe (L). Figure 10 provides the distribution of divertor target probes with small pink circles and numerical labels indicating their positions corresponding to the vertical coordinates of figure 9. There are 16 probes on the HFS target from bottom (mark 16) to top (mark 1), 14 probes on the bottom target from left (mark 17) to right (mark 30), and 13 probes on the LFS target from bottom (mark 31) to top (mark 43). The displacement of strike points could be inferred from these probe distributions and the intensity of their ion saturation currents. The ion saturation

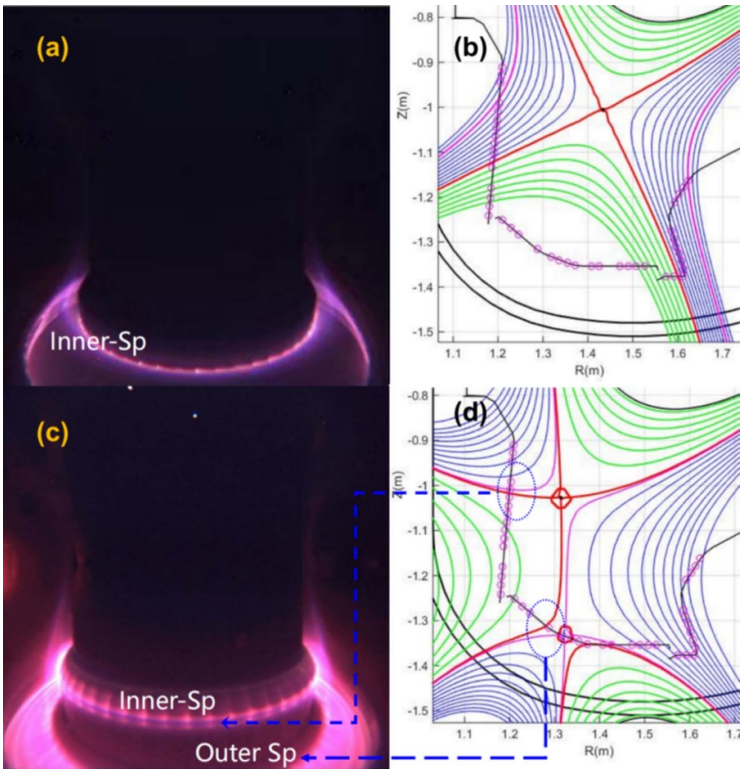

Figure 7. Image of the fast camera for SN discharge (*a*) and SF one (*c*), SN (*b*) and SF (*d*) divertor configuration. The bright rings in (*a*) and (*c*) are the strike points. The encircled areas are the outer divertor leg with great flux surface expansion, see in (*c*).

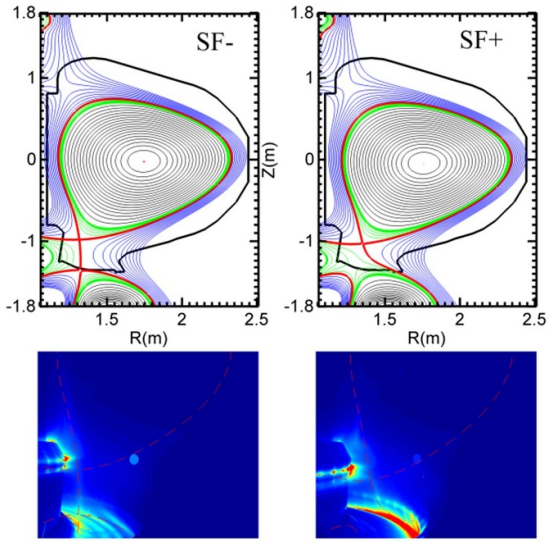

Figure 8. The divertor configurations reconstructed by EFIT and the corresponding visible images.

current on divertor target probe at the high field side (HFS) with the inner strike point is shown in figure 9(*c*). It is observed from the figure that the current becomes stronger when the $L > 25$ cm, indicating that the striking point is near the top of the inner target plate. The ion currents on the bottom and low-field side (LFS) target plates are shown in figures 9(*a*) and (*b*), respectively.

The outer strike point is scanned between the bottom and LFStarget plates, with different equilibrium configurations for phases (I) SF−, (II) SF+, and (III) SF−. Within the phase (I) from 800 ms to 950 ms, the strongest current is located at the HFS of bottom plate, where the outer strike point presents. At the same time, there is still a large current in the LFS of bottom plate. Such current distribution is caused by the joint action of the expansion of the flux surface and the secondary X-point. Meanwhile, the current on the LFS target plate is very weak. Therefore, the SF- configuration can be inferred. For phase (II) from 950 ms to 1250 ms, there is a notable decrease in ion current at the bottom plate, while simultaneously, a stronger current is observed on the LFS plate. This observation strongly supports an SF+ configuration. For the phase (III) from 1250 ms to 1600 ms, the current on the LFS target plate becomes stronger due to the auxiliary heating. However, there are still large current in the whole bottom, probably implying the SF- configuration. These inferences can be confirmed by the EFIT equilibrium reconstructions in figure 10. Three different configurations correspond to the phase (I), (II) and (III) in figure 9, as shown in figures 10(*a*)–(*c*), respectively. The positions of the inner and outer strike points in figure 10 are consistent with those inferred in figure 9. Moreover, the current distribution in the phase (III) is relatively stable, indicating that even during the auxiliary heating, the SF- configuration stabilizes for more than 300 ms.

Additionally, the superiority of the SF configuration in mitigating heat flux was vividly demonstrated by an infrared thermography [28] with spatial and temporal resolutions of

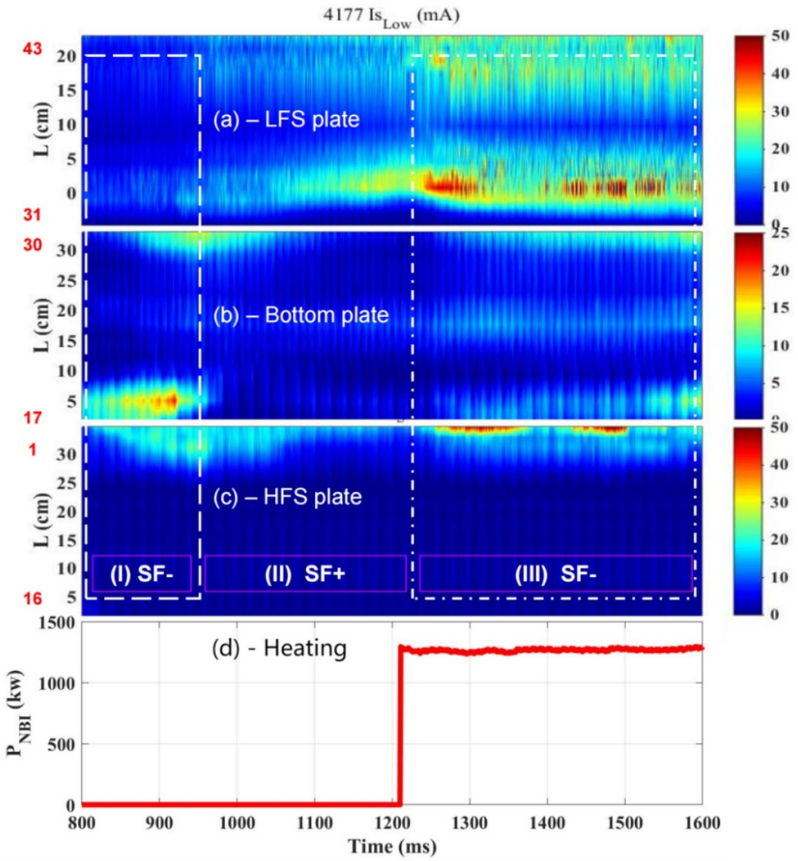

Figure 9. Time evolution of ion saturation current on diverter target probes for shot 4177, horizontal coordinate is time, while vertical coordinate represents the arc length along the target plate. (*a*) At the low field side (probes 31–43), (*b*) on the bottom plate (probes 17–30), (*c*) at the high field side with an inner strike point (probe 1–16), and (*d*) waveform of the NBI power. The outer strike point is scanned between the bottom area and low field side of the target plates, with different equilibrium configurations at (I) SF−, (II) SF+, and (III) SF- phases.

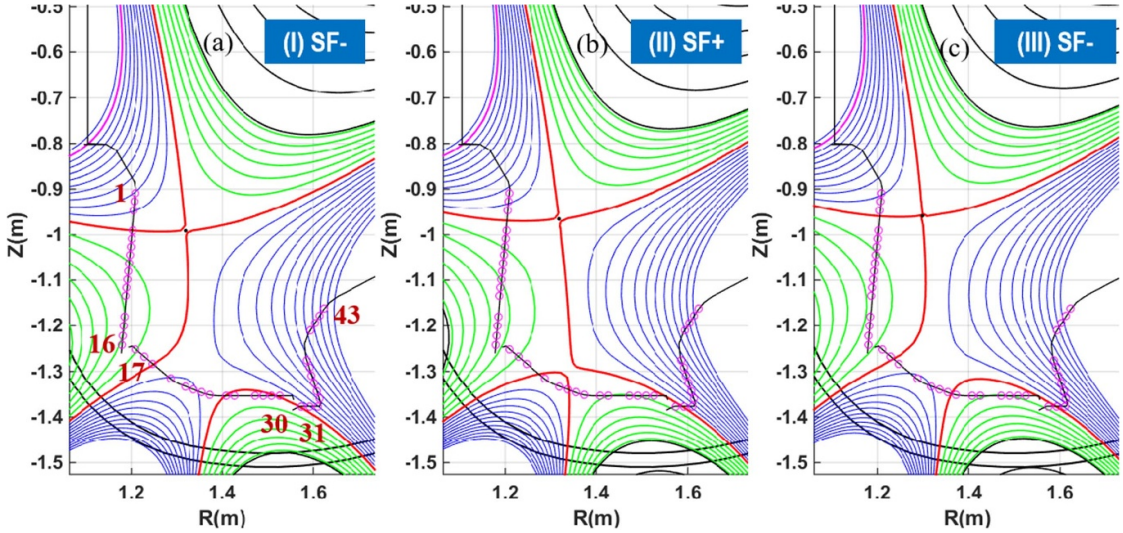

Figure 10. The equilibrium configurations (*a*) SF−, (*b*) SF+, and (*c*) SF−, correspond to the (I) SF−, (II) SF+, and (III) SF− phases in figure 9. The pink circles are the probes in divertor target with the number sequences. There are 16 probes on the high field side target from bottom (mark 16) to top (mark 1), 14 probes on the bottom plate from left (mark 17) to right (mark 30), and 13 probes on the lower field side target from bottom (mark 31) to top (mark 43).

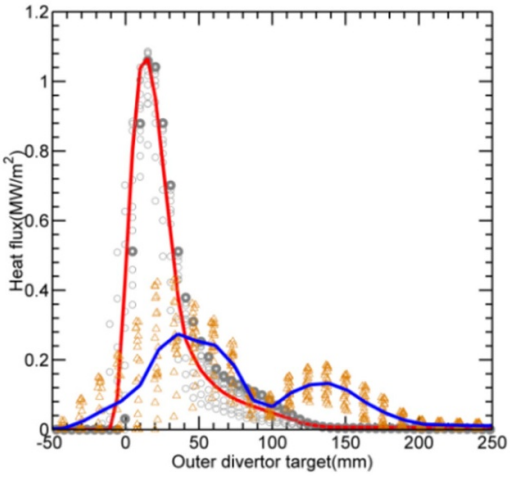

Figure 11. Contrast of divertor heat fluxes between SN (red line, #1737) and SF (blue line, #1797). The heat flux profiles are averaged using the data in 50 ms. The circles and the triangles are experimental data of the heat fluxes of SN and SF, respectively, measured by infrared thermography. The solid lines are their fitted results.

about 7 mm and 5 ms, respectively. It clearly showed that the peak heat flux in the SF was much lower than that in the SN, see figure 11.

As evidenced by observations from the HL-3 experiment, the SF divertor configuration exhibits superior control ability on target heat loading to the SN configuration. To delve deeper into the underlying physical mechanisms, a preliminary simulation study was conducted. This simulation harnessed the capabilities of the edge plasma code SOLPS-ITER [29–31], which was coupled with the fluid code B2.5 and the neutral transport code EIRENE.

The modeling main parameters based on the HL-3 standard and SF- experimental discharge parameters are presented below. The power entering into SOL heat flux is 840 kW, based on the experimental heat power and energy balance. The interface between inner core and SOL plasma density is fixed as $0.8 \times 10^{19}\,\mathrm{m}^{-3}$. The presence of carbon impurity was considered, attributed to the HL-3 carbon target plate [32]. The chemical sputtering factor is set as 0.03 at target surface. The pumping hole particle recycling coefficients is set as 0.95 to ensure the particle balance. The meshes for the standard divertor (SD) and SF- divertor configurations were generated using the HL-3 given discharge magnetic field information. The computational meshes comprise 96 poloidal and 36 radial cells in all modeling cases. The particle species considered in the code consist of D, D_2, C neutrals, D^+, D^{2+}, and C^{+1} to C^{+6} ions, along with electrons. The preliminary SOLPS-ITER modeling results have demonstrated that the HL-3 SF- can effectively reduce the perpendicular heat flux on the target. The detail comparison of target heat flux control between the snowflake SF- and SD is currently underway through a combination of experimental measurements and SOLPS-ITER numerical by considering the all drifts and currents [33].

The analysis yielded the following insights:

(i) Notably, the pitch angle of the magnetic field lines in the SF configuration is smaller than that in the SN configuration, as depicted in figure 13. Consequently, the perpendicular heat flux experienced by the target plate can be further reduced in the case of the SF divertor $q_{\mathrm{perp}} = q_{//}.\sin(\theta)$, here θ is pitch angle between the magnetic field line and target surface.

(ii) The SF configuration serves to disperse the target plate particles, leading to a significant increase in the contact area between the plasma and the target plate. The particle flux dispersed and contact area increased effectively diminishes the heat flux, as evidenced in figure 9(*b*).

(iii) The SF divertor effectively acts as a shield against the physical and chemical sputtering of the target plate by radiation carbon impurity particles. Thus, we can note that the core region carbon impurity density for SF is much less than conventional divertor (figures 12(*b*) and (*d*)). However, we can note that the total radiation power for the SF divertor (154 kW) is less than that for conventional close divertor (271 kW). Due to the weak particle flux on SF divertor target (see figure 9), the carbon impurity sputtering yield is lower than that of the conventional close divertor. Thus, this can further confirm that the SF with larger magnetic expansion and smaller pitch angle plays a more important role on the heat flux control.

These findings collectively shed light on the advantageous characteristics of the SF divertor in mitigating target heat loading and provide valuable insights into the underlying physics governing this phenomenon.

4. High confinement mode operation

In the year 2023, the HL-3 experiment achieved notable success by attaining H-mode discharges across three distinct configurations of primary parameters. The major radius is $R = 1.72$ m, the minor radius is in the range from $a = 0.55$–0.60 m. The toroidal magnetic field strength ranged approximately from $B_t = 1.6$–1.7 T, and the plasma current Ip exhibited variability between 500 kA and 1 MA. Despite the designated total rated auxiliary heating power in this phase being 11 MW, the recently installed auxiliary heating systems necessitate a commissioning period to achieve optimal power output. Notably, in the course of this experimental campaign, both NBI heating power and ECRH power have demonstrated capabilities exceeding 1 MW. Additionally, the contribution of LHW systems to the overall heating power is limited to a magnitude in the order of a few hundred kilowatts. Contemplating the absorption efficiency within the plasma, there arises a concern regarding the adequacy of heating power for facilitating the L-H transition. A predictive approach utilizing scaling laws

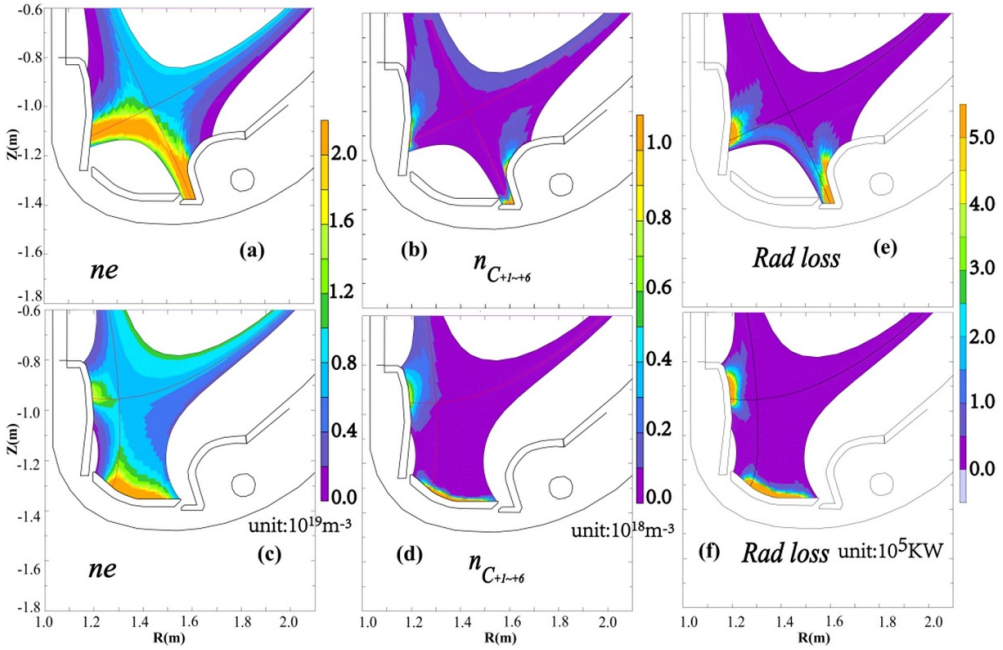

Figure 12. The electron density and carbon impurity density, and carbon impurity radiation loss distribution of conventional divertor *(a)*, *(b)* and snowflake minus divertor *(c)*, *(d)* from SOLPS-ITER modeling with the same upstream electron density and temperature.

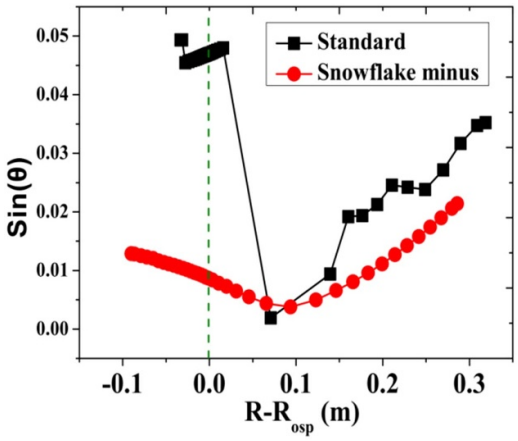

Figure 13. The pitch angle factor at target surface for Standard and snowflake minus divertors from SOLPS-ITER output. Here, Rosp is the outer striking point position.

was adopted to ascertain the L-H transition power, thereby identifying a minimal power threshold. The ITPA threshold database are deduced for each device from a data subset in which the high density branch is considered, and characterized by the Martin scaling law [34]:

$$\mathrm{P_{scal}} = 0.049\bar{\mathrm{n}}_{\mathrm{e}}^{0.72}\mathrm{B}^{0.80}\mathrm{S}^{0.94}.$$

Here $\bar{n}_{\mathrm{e}}$ is the line averaged density in the units of 10^{20} m^{-3}, B is the toroidal magnetic field in T and S is the plasma surface area in m^2. Conversely, the Ryter scaling law [35] posits the existence of a minimum transition density by introducing the low-density branch, reflecting diminished energy transfer from electrons to ions during dominant electron heating. The minimum density is described as:

$$n_{\mathrm{e,min}} = 0.7\mathrm{I}_{\mathrm{p}}^{0.34}B^{0.62}a^{-0.95}(R/a)^{0.4}.$$

In this formula, I_{p} is the plasma current in MA, R and a are major and minor radius in m. Substituting the expression for $n_{\mathrm{e,min}}$ into the ITPA threshold scaling provides a relation for the minimum power threshold:

$$p_{\mathrm{L-H}}^{\mathrm{min}} = 0.36\mathrm{I}_{\mathrm{p}}^{0.27}B^{1.25}R^{1.23}(R/a)^{0.08}.$$

According to the experimental parameters on HL-3, minimum power threshold relation suggests that only 1 MW power is required for the L-H transition in HL-3 experiments. The auxiliary heating power predominantly comprises NBI and ECRH power, with a nominal contribution of 100–200 kW from LHW power. Rigorous efforts are undertaken to maximize auxiliary heating power during all H-mode discharges, with the maximum value reaching approximately 2.5 MW. Throughout the experiments, variation of the line-averaged density is undertaken to pinpoint the minimum power threshold required for sustaining the desired operational mode. It cannot be definitively concluded that the density observed during the transition, corresponding to a minimum power threshold, is accurate, primarily due to the limitations of the existing database. Additionally, other influential factors during this transition, such as the presence of impurities and the divertor configuration may also play a significant role. The presented results indicate that the transition density appears to fall within a comparable range during the density scanning for

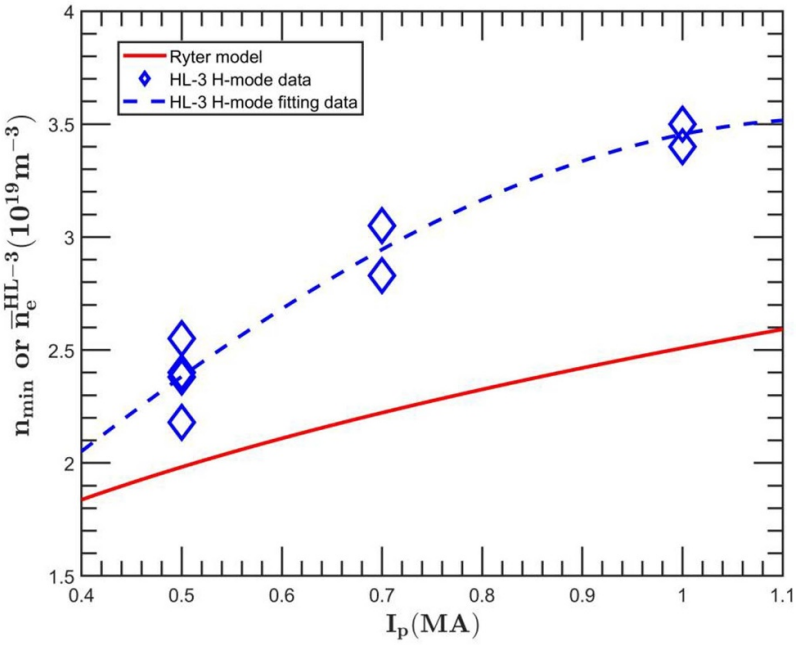

Figure 14. Comparison of the densities of HL-3 H-mode experiments with Ryter model [2]. The blue dash line is the fitting result of the HL-3 experiment data.

specific plasma currents, as depicted in figure 14. This suggests that a favorable density condition in HL-3 might exceed the predictions based on Ryter scaling. However, drawing a conclusive inference necessitates further data acquisition and a thorough investigation of potential underlying mechanisms. A common knowledge proposes that the sheared flow induced by the Er profile plays a crucial role in this phenomenon, a hypothesis substantiated by experimental validations [36–39]. The identification of an Er gradient threshold during the L-H transition reveals that the ion pressure gradient typically exerts dominance, accompanied by variations in ion heat flux and edge density profiles [40–42]. It should be emphasized that the influence of electron heat flux manifests subtly. Therefore, the collision rates between electrons and ions, as well as the associated energy transfer processes, assume significance, particularly in scenarios involving electron heating.

The power threshold for the L-H transition P_{LH} is characterized either by $P_{\mathrm{loss}} = P_{\mathrm{ohm}} + P_{\mathrm{aux}} + P_{\mathrm{alpha}}\text{-}\mathrm{d}W_{\mathrm{dia}}/\mathrm{d}t$ or by $P_{\mathrm{sep}} = P_{\mathrm{loss}}\text{-}P_{\mathrm{rad}}$. Here, P_{aux} is the total auxiliary heating power provided by the NBI, ECRH and LHW, P_{ohm} is determined from the loop voltage and plasma current, P_{alpha} is the α power assuming to be 0 in these discharges. W_{dia} signifies the plasma diamagnetic energy, P_{rad} is the radiation power, which is obtained from the 48 channels AXUV detectors covering the entire plasma profile.

Figures 15(*a*) and (*b*) present the data for HL-3 L-H transition power versus the center line-averaged electron density, analyzed separately using P_{loss} and P_{sep}. The Ryter scaling model is included in both figures for comparative purposes. Notably, the transition power observed in HL-3 appears to surpass the predictions based on the scaling law. This discrepancy could be attributed to an increase in radiation power during higher plasma current discharges in HL-3, aligning P_{sep} more closely with the expected scaling law trends. Several factors may contribute to the observed deviation of L-H transition power from the scaling model. Chief among them is the unidentified heating efficiency, which requires further exploration. Additionally, a higher fraction of electron heating may necessitate increased heating power, a hypothesis that could be tested through H-mode operation with NBI heating in the upcoming experimental campaign featuring elevated NBI power. In addition, the plasma radiation is underestimated with AXUV detector, typically 2–3 times comparing thermal bolometers, because the AXUV spectral response is not constant at energies ∼7–100 eV, and the AXUV suffers from a deterioration over time [43–45].

The temporal evolution of plasma parameters during a representative 1 MA H-mode discharge, specifically shot #4077, is shown in figure 16. The total auxiliary heating power is about 2.4 MW, provided by neutral beam injection (NBI), electron cyclotron resonance heating (ECRH), and the lower hybrid current drive (LHCD) as shown in figure 16(*b*). The line-averaged electron density depicted in figure 16(*c*) exhibits a gradual increase as a result of controlled density scanning through fueling prior to the L-H transition, alongside a consistent heating power after 1300 ms. The L-H transition is characterized by the sudden drop in D_α intensity in the divertor, as shown in figure 16(*d*). The transit time is marked by the vertical dashed line. After the L-H transition, noteworthy increments are observed in both the central line-averaged electron density (depicted in figure 16(*c*)) and plasma stored energy (depicted in figure 16(*e*)). Additionally,

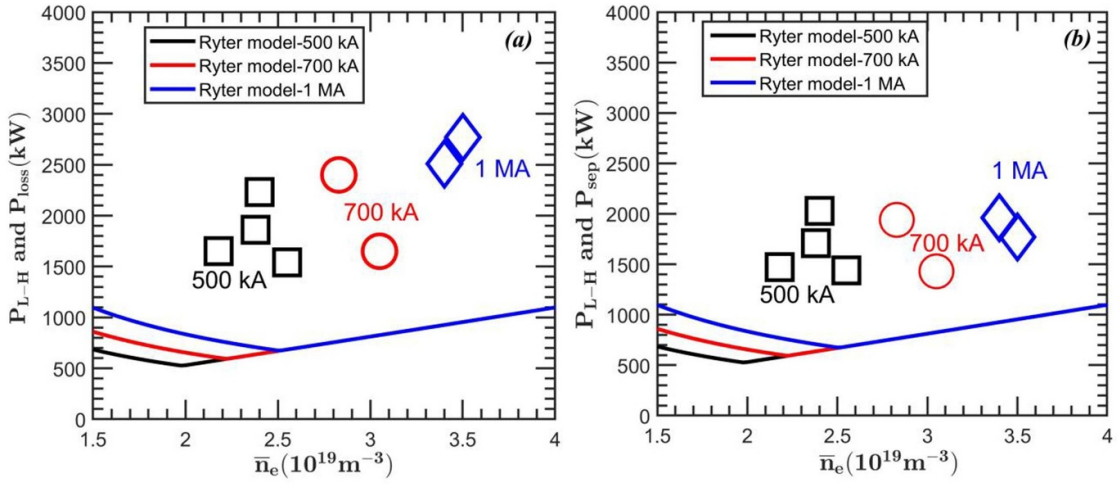

Figure 15. Comparisons of L-H transition power in HL-3 and Ryter mode, (*a*) $P_{\rm loss}$, (*b*) $P_{\rm sep}$ versus the center line-averaged electron density.

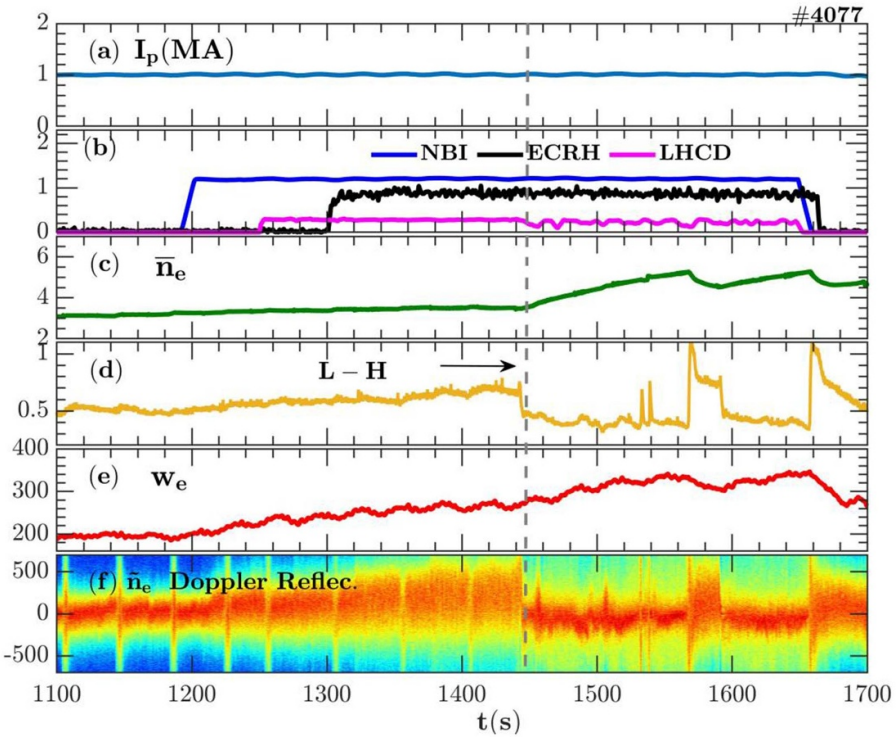

Figure 16. Time evolution of plasma parameters for H-mode discharge #4077: (*a*) plasma current, (*b*) power of NBI, ECRH, and LHCD, (*c*) central line-averaged electron density, (*d*) D_α intensity in the divertor, (*e*) plasma stored energy, (*f*) density fluctuation measured by Doppler reflectometry.

figure 16(*f*) showcases the decrement in edge density fluctuation, measured via Doppler reflectometry, during the H-mode phase, indicative of an enhanced plasma confinement. Figure 17 presents electron density profiles during L-mode (depicted in blue) and H-mode (depicted in red), wherein the pronounced density gradient during H-mode underscores the establishment of a particle transport barrier.

Notably, the 1 MA H-mode discharge was executed with a q95 value below 3, aligning with the ITER baseline scenario. It is anticipated that investigations into such discharges will augment the comprehensive dataset of ITER. The MHD activities are studied. Figure 18 elucidates the typical discharge waveforms with a q_{95} value of 2.75, with (*a*) spectrogram of the poloidal Mirnov signal, (*b*) divertor $D_{\rm a}$ and core $T_{\rm e}$ ($R = 165.9$ cm) signals, and (*c*) q profiles before (blue line) and after (red line) L-H transition which occurs at $t = 1442$ ms obtained from the EFIT reconstruction. It is observed that both the sawtooth crash and strong MHD activities manifest themselves both before and after the L-H transition, primarily attributable to the low central safety factor ($q_0 < 1$), as visually

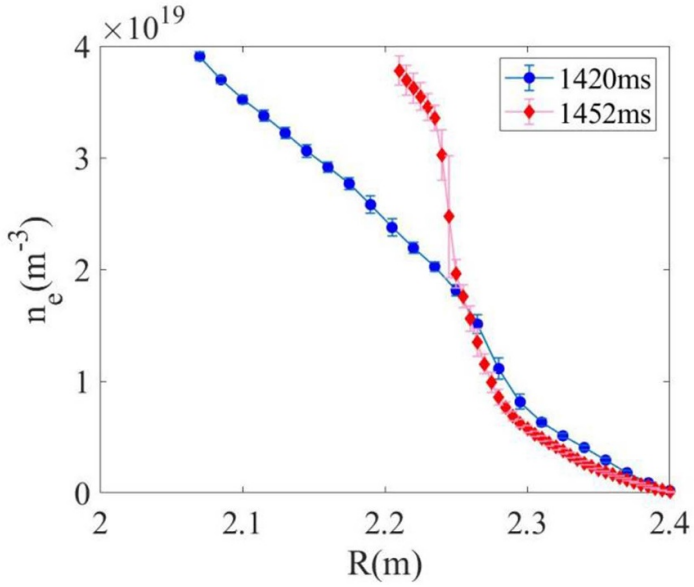

Figure 17. Electron density profiles for H-mode discharge #4077, L-mode phase (blue) and H-mode phase (red).

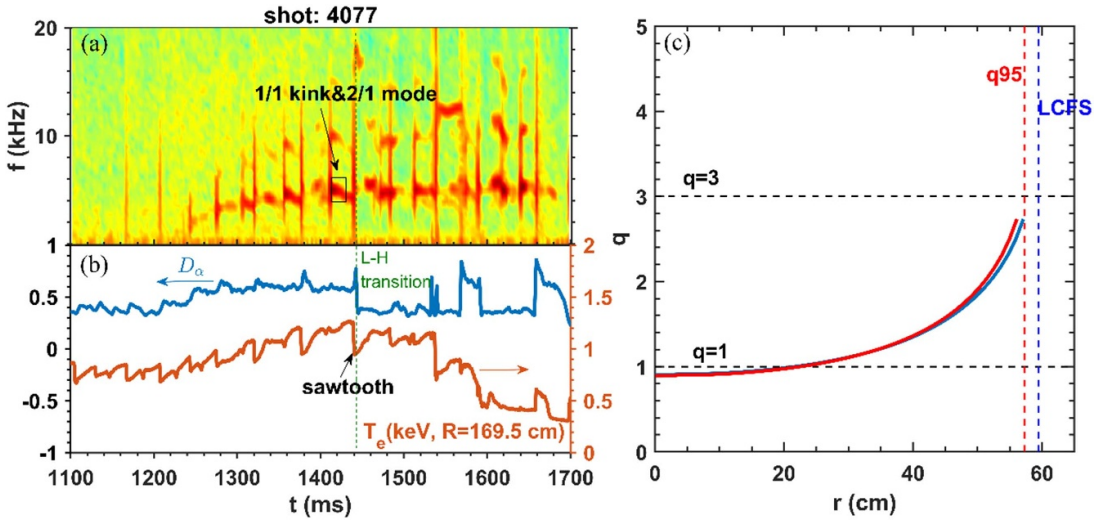

Figure 18. (*a*) Spectrum of Mirnov probe, (*b*) D_a signal and central T_e signal, and (*c*) q profiles before (blue line) and after (red line) L-H transition.

represented in figures 18(*b*) and (*c*). Of particular interest, a notable sawtooth event (at $t = 1439$ ms) materializes just prior to the L-H transition, as shown in figure 18(*b*), potentially triggered by the release of energy from the core to the plasma edge through the sawtooth mechanism.

Furthermore, an examination of the mode structure of MHD instabilities occurring between the sawtooth crashes has been undertaken. As illustrated in figure 19, radial profiles detailing the amplitude ($I_{\delta T_e/T_e}$) and phase ($\phi_{\delta T_e/T_e}$) of the relative electron temperature perturbation ($\delta T_e/T_e$) concerning a reference channel positioned at $R = 162.5$ cm are presented. The specific mode of interest is highlighted within a designated box in figure 18(*a*), corresponding to the time interval $t = 1412$–1419 ms, featuring a central frequency of approximately 5 kHz—situating it between two consecutive sawtooth crashes. Further analysis reveals the prevalence of the $m = 1$ kink mode in the core plasma, as depicted in figure 19(*a*). This mode exhibits kink behavior, evidenced by nearly constant phases (in phase) within the regions of strong mode intensity—namely, $R = 149$–163 cm on the HFS and $R = 180$–194 cm on the LFS (refer to figure 19(*b*)). The observation aligns with the conventional sawtooth precursor mode observed previously in other tokamaks [46, 47]. It should be also noted that an additional $m = 2$ mode perturbation ($m/n = 2/1$) is identified, as corroborated by Mirnov coil signals, in the outer region. This is exemplified by a significant variation of $I_{\delta T_e/T_e}$ in the vicinity of $R = 197$ cm and a corresponding phase flip at $R = 197$ cm. A more compre-

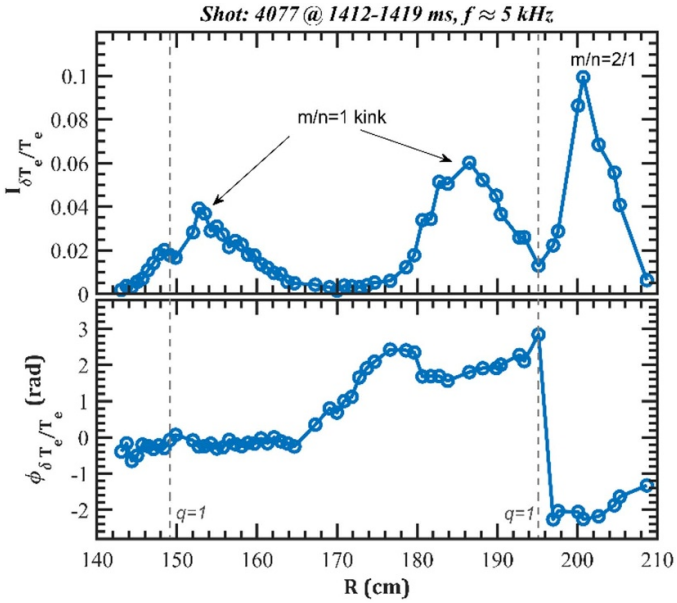

Figure 19. Radial profiles of the amplitude ($I_{\delta T_e/T_e}$) and phase ($\phi_{\delta T_e/T_e}$) of the relative electron temperature perturbation ($\delta T_e/T_e$) relative to a reference location at $R = 162.5$ cm. The MHD mode concerned is illustrated by the box in figure 18(*a*).

hensive exploration of the intricate MHD activities during low q H-mode operation and their impact on plasma confinement will be expounded upon in a subsequent, independent paper.

5. Summary

In the 2nd HL-3 experimental campaign (2022–2023), significant operation milestones of the machine were achieved. The divertor plasma was realized with plasma current $I_p \sim 1.2$ MA. For the first time, a 1 MA plasma H-mode was achieved through the combination of NBI, ECRH, and LHCD. The experiment demonstrated the advantages of the SF- diverted plasma discharge in heat flux control. The commissioning experiments of the 2nd campaign confirmed excellent capability for high-performance operation and advanced divertor study on HL-3. To enhance plasma performance and divertor heat flux mitigation, a double-null plasma configuration is being considered, along with the design and installation of an upper closed divertor in 2025. Over the next few years, experiments will focus on stably achieving triple production to 10^{20} m^{-3}keVs and ion temperatures exceeding 10 keV with deuterium-deuterium plasma. The plasma current will be further increased to 2 MA, and high-performance operation regimes, such as the ITER baseline and hybrid scenarios, will be prioritized. Main MHD instabilities, such as edge localized mode, neoclassical tearing mode, resistive wall mode, VDEs, as well as disruption alerting and mitigation, will be studied and controlled. Additionally, the physics of advanced divertor concepts will be explored, including configuration, structure, plasma-wall interaction, and innovative divertor heat flux active control technologies using SMBI impurity injection and the fish-tail divertor. In order to better support key physics and technologies towards ITER burning plasma, HL-3 is planned to prepare deuterium-tritium experiment in the near future. Towards this target, the capability of auxiliary heating system for ions is being increased from 15 MW (the beam with energy of 80 keV, planned before) to 26 MW (the beam of 20 MW with energy of 120 keV and ICRH of 6 MW). From July 2024, the HL-3 site will be upgraded, towards D-T experimental target, focusing on the site renovation and the building modification, such as the heating, the vacuum, the diagnostic systems, the tritium system and the radiation protection systems. Currently, efforts are underway for the design and development of tritium circulation and confinement systems. HL-3 is expected to handle gram-level tritium inventory while ensuring efficient recycling of the fuel. In the first step of 2027, the trace-tritium experiments with the transient puffed injection will be considered. Then, 50–50 DT mixtures will be tried after a sufficiently preparation in future.

Acknowledgments

The authors would like to acknowledge all those who have contributed to the HL-3 and HL-2A projects. Special thanks to J.F. Artaud ([2]CEA IRFM), L. Chen ([3]Zhejiang University & [4]University of California), L. Delpech ([2]CEA IRFM), A. Ekedahl ([2]CEA IRFM), P.H. Diamond ([13]University of California San Diego), Y.H. Ding ([14]Huazhong University of Science and Technology), J. Garcia ([2]CEA IRFM), Z. Gao ([5]Tsinghua University), X.Y. Gong ([15]University of South China), Z.B. Guo ([16]Peking University), T.G. Hoang, M. Isobe ([7]NIFS), Y.Q. Liu ([8]GA), D. Mazon ([2]CEA IRFM), S. G.R. Mckee ([9]University of Wisconsin-Madison), S. Morita ([7]NIFS), Y. Peysson ([2]CEA IRFM), Z.Y. Qiu ([3]Zhejiang University), Y. Ren ([17]PPPL), R. Sharples ([18]Durham University), G.R. Tynan ([13]University of California San Diego), X.G. Wang ([19]Harbin Institute of Technology), Z.X. Wang ([6]Dalian University of Technology),

Y.H. Xu ([10]School of Physical Science and Technology), Z. Yan ([9]University of Wisconsin-Madison), G. Zhuang ([11]University of Science and Technology of China), F. Zonca ([12]Center for Nonlinear Plasma Science and ENEA), X.L. Zou ([2]CEA IRFM) for their contributions to the physics modeling, experiments and diagnostic development. Partially, this work was supported by the National MCF Energy R&D Program under Grant Nos. 2022YFE03020000, 2022YFE03020001.

ORCID iDs

M. Xu https://orcid.org/0009-0001-3059-7026
W. Chen https://orcid.org/0000-0002-9382-6295
G.Q. Dong https://orcid.org/0000-0002-4289-4060
J.M. Gao https://orcid.org/0000-0002-9546-5139
G.Z. Hao https://orcid.org/0000-0003-2310-6134
R. Ke https://orcid.org/0000-0003-0117-0098
T. Long https://orcid.org/0000-0002-0136-8953
P.W. Shi https://orcid.org/0000-0002-2071-7741
S. Wang https://orcid.org/0000-0001-6480-7004
Z.Y. Yang https://orcid.org/0009-0000-4083-1552
L.M. Yu https://orcid.org/0000-0002-1177-3063

References

[1] Duan X.R. *et al* 2022 *Nucl. Fusion* **62** 042020
[2] Li Q. *et al* (HL-2M Team) 2015 *Fusion Eng. Des.* **96** 97338
[3] Zheng G.Y., Xu X.Q., Ryutov D.D., Xia T.Y., Duan X.R., He H.D. and Pan Y.D. 2016 *Fusion Eng. Des.* **112** 450
[4] Xue L., Duan X.R., Zheng G.Y., Liu Y.Q., Dokuka V.N., Lukash V.E. and Khayrutdinov R.R. 2017 *Nucl. Fusion* **57** 056029
[5] Xue L. *et al* 2023 *29th IAEA Fusion Energy Conf.* (*London, UK, 16–21 October 2023*) p 2138 (available at: https://www.iaea.org/sites/default/files/23/10/cn-316_fec_preliminary_program.pdf)
[6] Dong G.Q. *et al* 2023 *29th IAEA Fusion Energy Conf.* (*London, UK, 16–21 October 2023*) p 2079 (available at: https://www.iaea.org/sites/default/files/23/10/cn-316_fec_preliminary_program.pdf)
[7] Song X. *et al* 2021 *Nucl. Fusion* **61** 086010
[8] Li B., Song X., Xue L., Li J.X., Wang S., Song X.M., Zhang J.H. and Liu Y.Q. 2019 *Fusion Eng. Des.* **147** 111229
[9] Zhong W.L. *et al* 2023 *29th IAEA Fusion Energy Conf.* (*London, UK, 16–21 October 2023*) p 2340 (available at: https://www.iaea.org/sites/default/files/23/10/cn-316_fec_preliminary_program.pdf)
[10] Chen W. *et al* 2023 *29th IAEA Fusion Energy Conf.* (*London, UK, 16–21 October 2023*) p 2080 (available at: https://www.iaea.org/sites/default/files/23/10/cn-316_fec_preliminary_program.pdf)
[11] Shi P.W. *et al* 2023 *29th IAEA Fusion Energy Conf.* (*London, UK, 16–21 October 2023*) p 2050 (available at: https://www.iaea.org/sites/default/files/23/10/cn-316_fec_preliminary_program.pdf)
[12] Zhang N. *et al* 2023 *29th IAEA Fusion Energy Conf.* (*London, UK, 16–21 October 2023*) p 2246 (available at: https://www.iaea.org/sites/default/files/23/10/cn-316_fec_preliminary_program.pdf)
[13] Xiao G.L. *et al* 2023 *29th IAEA Fusion Energy Conf.* (*London, UK, 16–21 October 2023*) p 2168 (available at: https://www.iaea.org/sites/default/files/23/10/cn-316_fec_preliminary_program.pdf)
[14] Zhu Y.R. *et al* 2023 *29th IAEA Fusion Energy Conf.* (*London, UK, 16–21 October 2023*) p 2191 (available at: https://www.iaea.org/sites/default/files/23/10/cn-316_fec_preliminary_program.pdf)
[15] Gao J.M. *et al* 2023 *29th IAEA Fusion Energy Conf.* (*London, UK, 16–21 October 2023*) p 2219 (available at: https://www.iaea.org/sites/default/files/23/10/cn-316_fec_preliminary_program.pdf)
[16] Zhang Y.P. *et al* 2023 *29th IAEA Fusion Energy Conf.* (*London, UK, 16–21 October 2023*) p 2120 (available at: https://www.iaea.org/sites/default/files/23/10/cn-316_fec_preliminary_program.pdf)
[17] Chen H.T. *et al* 2023 *29th IAEA Fusion Energy Conf.* (*London, UK, 16–21 October 2023*) p 2336 (available at: https://www.iaea.org/sites/default/files/23/10/cn-316_fec_preliminary_program.pdf)
[18] Liu Y. *et al* 2023 *29th IAEA Fusion Energy Conf.* (*London, UK, 16–21 October 2023*) p 2131 (available at: https://www.iaea.org/sites/default/files/23/10/cn-316_fec_preliminary_program.pdf)
[19] Yang Z.Y. *et al* 2022 *Fusion Eng. Des.* **182** 113223
[20] Soukhanovskii V.A. *et al* 2018 *Nucl. Fusion* **58** 036018
[21] Soukhanovskii V.A. *et al* 2017 *Plasma Phys. Control. Fusion* **59** 064005
[22] Piras F. *et al* 2009 *Plasma Phys. Control. Fusion* **51** 055009
[23] Piras F., Coda S., Duval B.P., Labit B., Marki J., Medvedev S.Y., Moret J.-M., Pitzschke A. and Sauter O. 2010 *Phys. Rev. Lett.* **105** 155003
[24] Zheng G.Y., Xu X.Q., Ryutov D.D., Pan Y.D. and Xia T.Y. 2014 *Fusion Eng. Des.* **89** 2621–7
[25] Liu L. *et al* 2022 *Rev. Sci. Instrum.* **93** 083512
[26] Liu L. *et al* 2019 *Fusion Eng. Des.* **143** 41–47
[27] Wu N. *et al* 2023 *Phys. Plasmas* **30** 012501
[28] Gao J.M. *et al* 2015 *J. Nucl. Mater.* **463** 697–700
[29] Veselova I., Kaveeva E., Rozhansky V., Senichenkov I., Poletaeva A., Pitts R.A. and Bonnin X. 2021 *Nucl. Mater. Energy* **26** 100870
[30] Wiesen S. *et al* 2015 *J. Nucl. Mater.* **463** 480–4
[31] Subba F., Coster D.P., Moscheni M. and Siccinio M. 2021 *Nucl. Fusion* **61** 106013
[32] Zheng G.Y., Cai L.Z., Duan X.R., Xu X.Q., Ryutov D.D., Cai L.J., Liu X., Li J.X. and Pan Y.D. 2020 *Nucl. Fusion* **56** 126013
[33] Pan O., Lunt T., Wischmeier M., Coster D. and Stroth U. 2020 *Plasma Phys. Control. Fusion* **62** 045005
[34] Martin Y.R. *et al* 2008 *J. Phys.* **123** 012033
[35] Ryter F., Barrera Orte L., Kurzan B., McDermott R.M., Tardini G., Viezzer E., Bernert M. and Fischer R. 2014 *Nucl. Fusion* **54** 083003
[36] Groebner R.J., Burrell K.H. and Seraydarian R.P. 1997 *Phys. Rev. Lett.* **64** 3015
[37] Burrell K.H. 1997 *Phys. Plasmas* **4** 1499
[38] Wagner F. 2007 *Plasma Phys. Control. Fusion* **49** B1
[39] Stroth U., Manz P. and Ramisch M. 2011 *Plasma Phys. Control. Fusion* **53** 024006
[40] Schmidtmayr M. *et al* 2018 *Nucl. Fusion* **58** 056003
[41] Ryter F. *et al* 2016 *Plasma Phys. Control. Fusion* **58** 014007
[42] Liang A.S. *et al* 2020 *Nucl. Fusion* **60** 092002
[43] Peterson B.J., Kostrioukov A.Y., Ashikawa N., Liu Y., Xu Y., Osakabe M., Watanabe K.Y., Shimozuma T. and Sudo S. (LHD Experiment Group) 2003 *Plasma Phys. Control. Fusion* **45** 1167
[44] Suzuki C. *et al* 2007 *Plasma Fusion Res.* **2** S106214
[45] Vershkov V.A. *et al* 2017 *Nucl. Fusion* **57** 102017
[46] Zhao K.J. *et al* 2013 *Nucl. Fusion* **53** 123015
[47] Shao L.M. *et al* 2020 *Phys. Lett.* A **384** 126184